TU Delft

Delft University of Technology

Reservoir monitoring using borehole radars to improve oil recovery
Suggestions from 3D electromagnetic and fluid modeling

Zhou, Feng; Miorali, Mattia; Slob, Evert; Hu, Xiangyun

DOI
10.1190/geo2017-0212.1

Publication date
2018

Document Version
Final published version

Published in
Geophysics

Citation (APA)
Zhou, F., Miorali, M., Slob, E., & Hu, X. (2018). Reservoir monitoring using borehole radars to improve oil recovery: Suggestions from 3D electromagnetic and fluid modeling. *Geophysics*, *83*(2), WB19-WB32. https://doi.org/10.1190/geo2017-0212.1

Important note
To cite this publication, please use the final published version (if applicable).
Please check the document version above.

Copyright
Other than for strictly personal use, it is not permitted to download, forward or distribute the text or part of it, without the consent of the author(s) and/or copyright holder(s), unless the work is under an open content license such as Creative Commons.

Takedown policy
Please contact us and provide details if you believe this document breaches copyrights.
We will remove access to the work immediately and investigate your claim.

This work is downloaded from Delft University of Technology.
For technical reasons the number of authors shown on this cover page is limited to a maximum of 10.

GEOPHYSICS, VOL. 83, NO. 2 (MARCH-APRIL 2018); P. WB19–WB32, 15 FIGS., 4 TABLES.
10.1190/GEO2017-0212.1

Check for updates

Downloaded 01/25/18 to 131.180.130.242. Redistribution subject to SEG license or copyright; see Terms of Use at http://library.seg.org/

Reservoir monitoring using borehole radars to improve oil recovery: Suggestions from 3D electromagnetic and fluid modeling

Feng Zhou[1], Mattia Miorali[2], Evert Slob[2], and Xiangyun Hu[3]

ABSTRACT

The recently developed smart well technology allows for sectionalized production control by means of downhole inflow control valves and monitoring devices. We consider borehole radars as permanently installed downhole sensors to monitor fluid evolution in reservoirs, and it provides the possibility to support a proactive control for smart well production. To investigate the potential of borehole radar on monitoring reservoirs, we establish a 3D numerical model by coupling electromagnetic propagation and multiphase flow modeling in a bottom-water drive reservoir environment. Simulation results indicate that time-lapse downhole radar measurements can capture the evolution of water and oil distributions in the proximity (order of meters) of a production well, and reservoir imaging with an array of downhole radars successfully reconstructs the profile of a flowing water front. With the information of reservoir dynamics, a proactive control procedure with smart well production is conducted. This method observably delays the water breakthrough and extends the water-free recovery period. To assess the potential benefits that borehole radar brings to hydrocarbon recovery, three production strategies are simulated in a thin oil rim reservoir scenario, i.e., a conventional well production, a reactive production, and a combined production supported by borehole radar monitoring. Relative to the reactive strategy, the combined strategy further reduces cumulative water production by 66.89%, 1.75%, and 0.45% whereas it increases cumulative oil production by 4.76%, 0.57%, and 0.31%, in the production periods of 1 year, 5 years, and 10 years, respectively. The quantitative comparisons reflect that the combined production strategy has the capability of accelerating oil production and suppressing water production, especially in the early stage of production. We suggest that borehole radar is a promising reservoir monitoring technology, and it has the potential to improve oil recovery efficiency.

INTRODUCTION

Ground-penetrating radar (GPR), usually working in frequencies from tens of MHz to several GHz, has been widely applied in mapping near-surface geologic structures (Daniels et al., 1988). High-frequency electromagnetic (EM) waves are sensitive to water content due to the great contrast of permittivity between water and other soil or rock components. Therefore, GPR can be applied in groundwater assessment. Especially, a time-lapse GPR measurement method is widely used to monitor the migration of water or steam in shallow (tens of meters) fractures or vadose zones (Tsoflias et al., 2001; Huisman et al., 2003; Talley et al., 2005). To overcome the limitation of surface GPR, borehole radar is used by deploying antennas under the surface (Sato and Takayama, 2007; Kuroda et al., 2009). Cross-hole, single-hole, and vertical radar profiling measurements have been conducted for fracture and cavity detection, metal ore exploration, and underground water assessments (Zhou and Sato, 2000, 2004; Ellefsen et al., 2011; Tronicke and Hamann, 2014; Yang et al., 2015). Some novel types of GPR antennas have been designed suitable for downhole materials and structures. A typical example is polarimetric borehole radar, which can estimate target orientation and fracture roughness (Zhao and Sato, 2006, 2007, 2008). In the currently available applications, borehole radars are deployed at a depth of tens to hundreds of meters under the

Manuscript received by the Editor 9 April 2017; revised manuscript received 24 September 2017; published ahead of production 21 November 2017; published online 10 January 2018.
[1]China University of Geosciences (Wuhan), School of Mechanical Engineering and Electronic Information, Wuhan, China; Delft University of Technology, Department of Geoscience and Engineering, Delft, The Netherlands. E-mail: zhoufeng@cug.edu.cn.
[2]Delft University of Technology, Department of Geoscience and Engineering, Delft, The Netherlands. E-mail: mattia.miorali@gmail.com; e.c.slob@tudelft.nl.
[3]China University of Geosciences (Wuhan), Institute of Geophysics and Geomatics, Wuhan, China. E-mail: xyhu@cug.edu.cn.
© 2018 Society of Exploration Geophysicists. All rights reserved.

Downloaded 01/25/18 to 131.180.130.242. Redistribution subject to SEG license or copyright; see Terms of Use at http://library.seg.org/

ground. Even deeper applications of GPR technology, for example, hydrocarbon reservoirs at a depth of up to thousands of meters, have been proposed (Chen and Oristaglio, 2002; Heigl and Peeters, 2005). Recently, laboratory experiments have been conducted to emulate the EM response of a wideband radar on the perforations and impairments of an oil well (Oloumi et al., 2015), and a borehole radar prototype system is under development for well logging usage (Ma et al., 2016).

Current studies for GPR applications in oil fields have mainly focused on hydrocarbon exploration activities, in which radar antennas are designed in a logging string or drill collar for wireline logging or logging-while drilling (LWD), respectively (Heigl and Peeters, 2005; Guo and Liu, 2010; Liang et al., 2013). However, in our view, another potential application of GPR in oil fields resides in hydrocarbon development activities. In this application, downhole GPR is thought to have capability of monitoring the movement of water and oil, and it can help to improve oil recovery efficiency when combined with a so-called smart well.

The smart well (or intelligent well) is an advanced well equipped with downhole sensors and inflow control valves (ICVs) to monitor and control hydrocarbon production (Glandt, 2005). The well is separated into several relatively independent segments or completions by packers between the casing and tubing. ICVs segmentally control the inflow of liquids from the casing to the tubing. The valves can be choked in a one-off, discretely variable, or infinitely variable mode. Downhole electrical cables or hydraulic conduits provide remote control to the valves from the surface (Konopczynski and Ajayi, 2004). Permanent downhole sensors continuously or semicontinuously monitor production status inside or outside the well, and the reservoir information is delivered to the surface control center through downhole communication systems (Dyer et al., 2007). Smart wellbore facilities have been developed, and early applications have demonstrated great attraction to the oil industries (Elmsallati et al., 2005). A simple structure of a typical smart wellbore is schematically presented in Figure 1. Combined with a suitable monitoring and control strategy, the smart well is capable of improving reservoir management and increasing recovery efficiency (Dilib et al., 2015).

However, a practical smart well optimization strategy is limited by poor knowledge of reservoir fluid behaviors. The task of smart well sensing technology is to acquire information from reservoirs or wells. With adequate reservoir dynamic information, data-driving feedback control strategies are realizable (Zhou et al., 2015). In general, the downhole monitoring can be categorized into in-well sensing and reservoir imaging. In-well sensors are currently technologically mature and have been installed in realistic smart wells (Dilib et al., 2015). Examples of successfully applied in-well monitoring techniques include pressure gauges, temperature sensors, and multiphase flow meters based on fiber optics (Kragas et al., 2003; Webster et al., 2006; Aggrey et al., 2007). These tools can only monitor fluid changes inside or closely adjacent to the well. For sensing far away from the well, reservoir imaging technology, whether on ground or downhole, is imperative. Surface 4D seismic has been used to characterize the distributions of remaining oil through the differences of data surveyed over time (Lumley, 2001). However, because of the long intervals of data acquirements (normally at a few years), the measurement backgrounds are usually changed, wherefore time-lapse data processing is difficult to produce the results with high accuracy, high resolution, and high signal-to-noise ratio (Watts et al., 2006). Permanently installed downhole geophones are expected to be able to indirectly locate the displacement front, but data interpretation is difficult because of the natural insensitivity of elastic waves on fluid components (Gagliardi and Lawton, 2012). To date, no downhole seismic has been permanently installed in a smart well system in spite of its successful applications to downhole fracturing monitoring (Silva et al., 2012). Four-dimensional gravity can infer density changes of fluids associated with hydrocarbon production, whereby it is viable in monitoring gas-water rather than oil-water displacement (Reitz et al., 2015). Nowadays, a downhole gravity tool exists only in a wireline logging mode, but a gravity monitoring tool permanently installed in the downhole is still unavailable (Black et al., 2016). Recent theoretical and experimental studies found that considerable signals of streaming potential, which respond to approaching water, are detectable in a production well, and the investigation distance ranges from tens of meters up to a few hundred meters (Vinogradov and Jackson, 2011). However, the measured magnitude is limited by the production rate, formation water salinity, and coupling coefficient between fluids and electric potential, among which the latter two are poorly understood (Saunders et al., 2012). These reservoir imaging techniques, even though some of them are under development, are suited only for large-scale (tens to hundreds of meters) water flooding monitoring with a low-resolution requirement. In addition, the responded signals are difficult to directly image the displacement front, and data interpretation is cumbersome and uncertain. So far, a proper tool does not exist to precisely resolve the near-well region from several to tens of meters. However, the monitoring of this region is strongly required in some specific production environments. Two examples are thin oil rims produced by horizontal wells and heavy oil reservoirs produced through steam-assisted gravity drainage (SAGD). Thin oil rim reservoirs are relatively thin oil columns (in an order of a few to tens of meters), sandwiched between water and gas or shale. In the case of horizontal well production, they often encounter early water breakthrough caused by reservoir heterogeneity and wellbore pressure drop (Jansen et al., 2002). SAGD is an enhanced oil recovery technology for heavy crude oil production. Two horizontal wells are parallelly drilled through the oil-bearing layer, with the upper for steam injection and the lower for heated oil collection (Butler, 1991). The main challenge is to let the steam chamber grow in a controllable way to reduce the production of steam or condensate water. In both recovery environments, an investigation depth of several meters away from the well can support production optimization by means of smart wells.

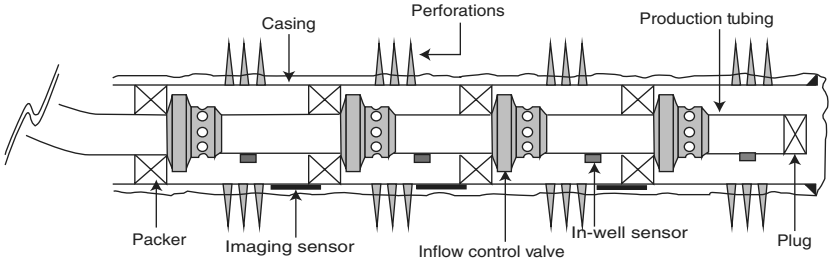

Figure 1. Schematic representation of a conceptual smart wellbore in horizontal well production. Downhole cables are not presented (Poel and Jansen, 2004).

Downloaded 01/25/18 to 131.180.130.242. Redistribution subject to SEG license or copyright; see Terms of Use at http://library.seg.org/

From a more general perspective, realistic reservoirs have heterogeneous permeability or contain fractures or channels, presenting an uneven displacement front when flooded or derived. The nonuniform displacement causes premature breakthrough of undesired fluids (e.g., water, gas, or steam), and it thus reduces oil production, especially in the case of horizontal well production. If downhole imaging techniques are capable of capturing fluid changes in the reservoirs, then they can support an effective production control with the smart well (Ebadi and Davies, 2006).

The objectives of production optimizations are to maximize oil production, minimize undesired fluid production, or gain an optimal net present value (Ebadi and Davies, 2006). The production controls with ICVs can be either reactive or proactive (or are termed "defensive"). Reactive control adjusts the settings of ICVs after the unwanted fluids invade the well, whereas proactive control responds to flow changes measured or predicted at a distance away from the well. Downhole multiphase flow meters are commercially available, which allows for in-well water cut measurements for reactive control. Early investigations showed that a proportional reactive control, employing continuously variable ICV settings for segmental inflow adjustment, can yield a neutral or positive economic return compared with the uncontrolled conventional well, flow-fixed segmented well, and on/off reactive control productions (Addiego-Guevara et al., 2008). Proactive control is hopeful to yield more benefits for its early warning to water invasion, whereas the applicability strongly depends on reservoir imaging technology. Currently, ongoing reservoir imaging techniques, as mentioned before, fail to monitor the near-well region (a few to tens of meters from the wells). Our previous work evaluated the feasibility of a GPR detecting water front based on EM propagation theory, and it suggested that in a relatively low-conductivity reservoir ($\sigma < 0.02$ S/m), a detection range of 10 m is obtainable (Miorali et al., 2011a, 2011b). Based on these, we propose that borehole radar might be an effective downhole monitoring tool to support a proactive control in a thin oil reservoir production.

This paper investigates the capability of borehole radars for imaging reservoirs and then quantifies its contributions to oil production. First, an integrated 3D numerical model is established by coupling multiphase flow and EM propagation modeling. The model imitates a bottom-water drive reservoir produced by a horizontal well in which radar antennas are installed. A box-scale simulation is implemented to investigate the capability of borehole radar detecting the water front in the way of time-lapse measurements. Second, to examine the effectiveness of borehole radar imaging, a reservoir-scale simulation is conducted in a thin oil rim scenario. An array of borehole radars is assumed to be distributed in a horizontal well, and the traces of received signals are gathered to image the advancing water front profile. Then, the imaging results are used to implement a proactive control procedure of smart well. Finally, to assess the potential benefits that borehole radars bring to oil production, three different production strategies are simulated and compared. A conventional well production, with no monitoring and control devices, is simulated as a reference case. The second production strategy adopts a proportional reactive control, which gradually adjusts ICVs after water breakthrough, and this control strategy is thought of as the optimum smart well production strategy in the currently technologically available level (Addiego-Guevara et al., 2008). The third production strategy combines proactive control with proportional reactive control, and it can adjust ICVs before and after water breakthrough. In this production strategy, in addition to multiphase flow meters, the well is equipped with reservoir monitoring tools, which can be supported by our borehole radars.

WATER FRONT MONITORING USING BOREHOLE RADAR

Flow modeling

Multiphase flow is simulated using an in-house reservoir simulator — Modular Reservoir Simulator (MoReS) (Regtien et al., 1995). The flow model (labeled as model 1) is a box-shaped oil-bearing reservoir sandwiched between a shale and an active aquifer, with dimensions of $100 \times 200 \times 42.5$ m^3. The heterogeneous porosity and permeability are similar to the scenario in MoReS-Atlas examples (Verbruggen, 2005). A horizontal well, with a surface production rate of 275 m^3/d, is located below the shale. The principal properties of fluids and rock are listed in Table 1, and capillary pressure is considered.

The reservoir model is discretized by nonuniform grids. The region in the proximity of the wellbore, $60 \times 20 \times 10$ m^3, is discretized with a cell size of $0.5 \times 0.5 \times 0.1$ m^3. The fine gridding scheme allows simulation of a realistic oil-water transition zone. The permeability and porosity in this region are magnified, as shown in Figure 2. Coarse gridding is applied outside this region with cell sizes of exponential growth for saving computing time and computer memory.

Radar modeling

We used GprMax, a GPR data simulator based on finite-difference time-domain (FDTD) method, to simulate EM waves propagating and scattering in the reservoir (Giannopoulos, 2005). The main properties affecting EM wave propagation are conductivity and permittivity of the mixed media. The oil-bearing layer consists of rock matrix, crude oil, and a small portion of connate water, among which the connate water is the primary contribution to

Table 1. Properties of fluids and rock for model 1.

Reservoir and well parameters		
Variables	Values	Units
Initial pressure at reference depth	10,000	kPa
Rock compressibility	2.00e-9	$(\text{kPa})^{-1}$
Water compressibility	4.35e-7	$(\text{kPa})^{-1}$
Oil compressibility	2.28e-7	$(\text{kPa})^{-1}$
Water density	999.50	kg/m^3
Oil density	888.40	kg/m^3
Water viscosity	5.00e-4	Pa · s
Oil viscosity	3.40e-4	Pa · s
Connate water saturation	0.25	—
Residual oil saturation	0.25	—
Water end-point relative permeability	0.80	—
Oil end-point relative permeability	0.80	—
Water Corey exponent	2	—
Oil Corey exponent	2	—

Downloaded 01/25/18 to 131.180.130.242. Redistribution subject to SEG license or copyright; see Terms of Use at http://library.seg.org/

EM propagation attenuation. As analyzed by Chen and Oristaglio (2002), reservoir conductivity is the primary constraint for borehole radar usage. Studies also found that, in a relatively high-resistivity reservoir (e.g., conductivity in an order of 10^{-2} S/m or less), when the frequency is above 100 MHz, attenuation and phase distortion become independent on frequency, and dispersion is negligible whereas attenuation is tolerable (Miorali et al., 2011a). Such a reservoir condition is readily satisfied in realistic oil fields, and thus it is a natural regime for a true radar measurement. In the meantime, the radar frequency is not suggested to exceed a few GHz to avoid dielectric relaxation caused by water molecular polarization (Donadille and Faivre, 2015). In the limited frequency bands, the lower operation frequency tends to achieve a larger detection range. Investigations showed that for a reservoir with a conductivity of 0.02 S/m, water-front reflection in the range of 10 m is detectable by a commercial GPR system with the center frequency of 100 MHz (Miorali et al., 2011b). We therefore adopt a center frequency of 100 MHz in our radar monitoring simulations, and the oil-bearing reservoir has a conductivity smaller than 0.02 S/m. Under these constraints, the materials in the reservoirs are treated as lossy and isotropic, and the constitutive parameters are frequency independent.

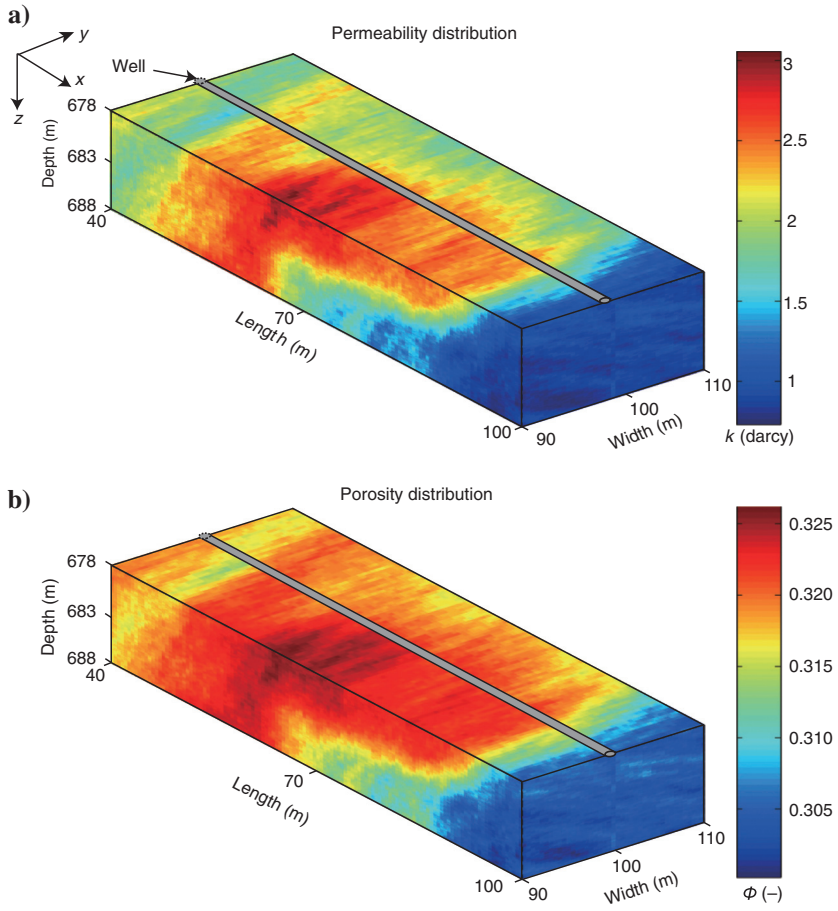

Figure 2. Horizontal permeability (Figure 2a) and porosity (Figure 2b) in the fine gridding region (the ratio of the vertical and horizontal permeabilities is 0.6).

Table 2. EM properties of the components in the reservoir and well.

EM properties		
Variables	Values	Units
Rock relative permittivity	7	—
Water relative permittivity	80	—
Oil relative permittivity	3	—
Water conductivity	1	S/m
Cementation exponent	2	—
Saturation exponent	2	—
Relative permittivity of filling material	30	—
Conductivity of filling material	1e-4	S/m

The comprehensive electric conductivity and permittivity are governed by the relative contents of each component in the saturated rock and their respective electric properties. Assuming the rock matrix consists of sandstone, the reservoir conductivity can be calculated by Archie' s law (Archie, 1942):

$$\sigma_t = \sigma_w S_w^n \phi^m, \tag{1}$$

where σ_t and σ_w, respectively, denote the electric conductivity of the saturated sandstone and the formation water, S_w is the water saturation, ϕ is the porosity, m is the cementation exponent of the rock, and n is the saturation exponent. The effective permittivity of the saturated rock is primarily dominated by the content of water for its permittivity that is much greater than that of rock and oil. The effective permittivity can be calculated with the complex refractive index model (CRIM), which is frequently used for geologic materials in the radar frequency (Birchak et al., 1974):

$$\epsilon_{\text{eff}} = [(1-\phi)\epsilon_s^{1/2} + \theta\epsilon_w^{1/2} + (\phi-\theta)\epsilon_o^{1/2}]^2, \tag{2}$$

where ϵ_o, ϵ_w, and ϵ_s are, respectively, the relative permittivity of oil, water, and rock matrix, and $\theta = \phi S_w$ is the volumetric fraction of the formation water per unit volume of rock. The electric properties of the components used in the EM modeling are presented in Table 2.

By means of the formulas mentioned above, the multiphase flow model can be coupled with the EM model, allowing to observe the correlations between the radar responses and the water front advancing. Figure 3 diagrammatically presents the coupling procedure. Through a sequence of joint simulations at a prescribed time interval, time-lapse EM signals can be extracted by the subtraction between two consecutive EM responses. The time-lapse borehole radar measurement is similar to the 4D seismic survey on the ground (Lumley, 2001), but downhole measurements are able to acquire high-resolution data. The time-lapse waveforms carry only

Downloaded 01/25/18 to 131.180.130.242. Redistribution subject to SEG license or copyright; see Terms of Use at http://library.seg.org/

the signals reflected from the changed portions of the reservoir caused by fluid flowing. The signals from the unchanged portions, including direct and reflected waves from the heterogeneous rock, are removed by the subtraction operation.

Although the method is theoretically feasible, a significant challenge remaining in field operations is how to install radar antennas in complicated downhole environments. To transmit and receive EM waves toward and from the formation, the radar antennas should be installed outside of the casing and be located as close to the formation as possible. For practical considerations, we propose to reshape the casing by attaching an additional metal bulge outside it and place the antennas inside the groove of the bulge, as depicted in Figure 4. The redesigned wellbore does not impair the mechanical strength of the casing, whereas it increases the contact of the antennas with the formation. Antennas are restricted in a wire dipole type due to the limited space available in the cross plane of the groove. However, another general problem is that the emitted EM signals are destructively interfered by the metal body. A solution is to fill a kind of highly dielectric material inside the groove to isolate antennas from the metal component. Our previous study testified that a specific insulating filler with a certain thickness can relieve the unfavorable interference from the metal casing (Miorali et al., 2011a). Ferrite is one of the proper filling materials for our application because it has similar electric properties to insulating materials as well as high mechanical strength like metal. The metal back cavity of the groove can act as a curved reflector behind the antenna, allowing for directional energy transmitting as well as directional signal collecting, as discussed by van Dongen et al. (2002). Some other technical issues, such as downhole power supply and data transmission, are not discussed here because permanent downhole gauges and optical fiber monitoring systems have been successfully applied in smart wells (Glandt, 2005). Radar transceiver modules are also possible to be installed in the limited downhole space with the development of microelectromechanical systems (Ren et al., 2014). Based on the clarifications, we believe that it will be technically achievable for borehole radars installed in a smart well.

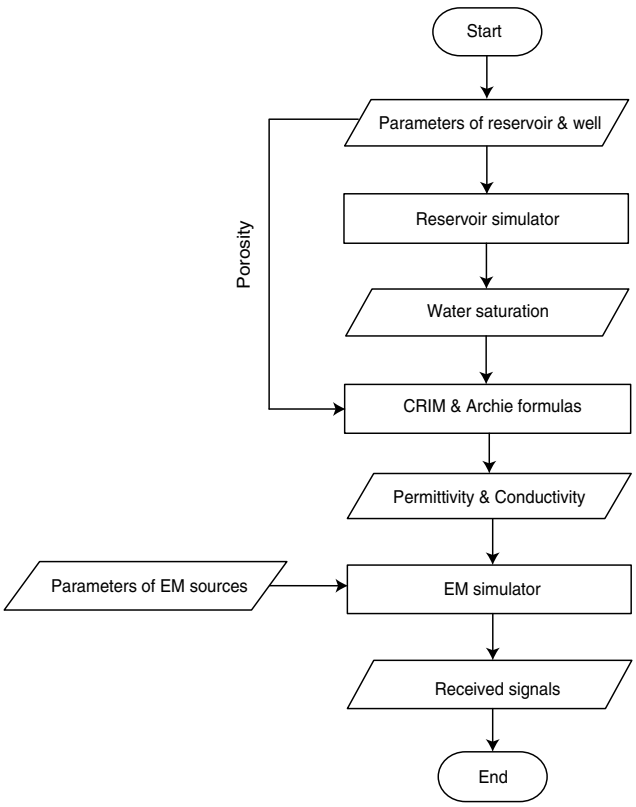

Figure 3. Flowchart of coupling multiphase fluid flow and EM propagation models.

In the EM simulations, the well casing is deemed as a perfect conductor, and the electric properties of the insulated filler and the formation components are presented in Table 2. The radar transmitter is treated as a Hertzian dipole source, fed by a first derivative of Gaussian pulse with a center frequency of 100 MHz. The antennas are bistatic, and the transmitter and receiver are separated by 1 m along the well. EM polarization is in the longitudinal direction of the well. The EM simulation domain is discretized by a cell size of $0.025 \times 0.025 \times 0.025$ m^3 to satisfy $\Delta l \leq \lambda/10$, where Δl denotes the cell size and λ the minimum wave length in the propagation media. Perfectly matched layer (PML) boundary conditions are exerted to model an open propagation space in a finite simulation domain.

EM responses

The reservoir model described above is simulated to demonstrate the dynamics of fluids in the production process, and then the EM model is run to observe the time-lapse radar responses on the movement of fluids. To decrease the computational cost of 3D EM simulations, a box volume of fluid distributions, with the dimensions of $5 \times 5 \times 10$ m^3, is extracted at the prescribed simulation time. The investigated region is located below the borehole radars, presenting fairly realistic oil-water transition zones due to the fine meshing.

Figure 5 shows the evolution of water saturation in the extracted box volume after 150 days, 165 days, 180 days, and 195 days of production, respectively. The corresponding 1D water saturation curves are extracted below the center of the EM source and receiver, as shown in Figure 6. A gradually varying oil-water transition zone is clearly observed, and the leading edge of water displacement is 8.7,

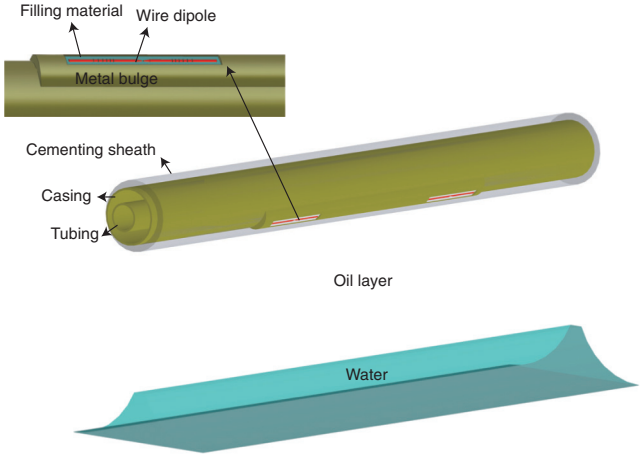

Figure 4. Schematic representation of the well configured by radar sensors in a water driving reservoir.

Downloaded 01/25/18 to 131.180.130.242. Redistribution subject to SEG license or copyright; see Terms of Use at http://library.seg.org/

6.8, 4.7, and 2 m away from the well, respectively. In the received signal components, the electric field component that is parallel to the well (i.e., E_x) has the largest response on the water front; thus, we only recorded time-lapse E_x components, as shown in Figure 7. The waveforms show a gradually strengthened refection event, and the first arrival is, respectively, at 158.8, 123.2, 81.7, and 31.9 ns, corresponding to the approaching water front (Figures 6 and 7). Note that other wave components, such as direct waves, residual metal interference, and background clutter arising from inhomogeneous rock pores, carry no useful signals in this application, and they have been mostly filtered by time-lapse operations. The contrast between water saturation profiles and time-lapse EM waveforms indicates that, with every passing 15 days, the water front moves forward 1.9, 2.1, and 2.7 m, respectively, and meanwhile the arrival time of the reflected wavelet, respectively, shortens 35.6, 41.5, and 49.8 ns, presenting a proportional change (Figures 6 and 7). The positive correlation of both events makes it possible to quantitatively estimate the position or movement speed of the water front in different production regions.

For quantitative characterizations of oil-water distributions, it is required to estimate the velocity of EM wave propagating in reservoirs, thereby converting the traveltime of radar recordings into distance or depth. There are various approaches for EM wave velocity estimation in GPR measurements, whereas we propose to estimate EM wave velocity through formation dielectric permittivity for our application cases. A direct way to acquire the reservoir permittivity is to measure coring samples with a coaxial-line sample holder, as demonstrated by Shen (1985). In addition, an indirect but cheap approach for formation permittivity acquirement is to use a so-called dielectric dispersion logging tool. This kind of wireline EM logging uses multispacing, multifrequency, and cross-polarization antenna arrays to measure attenuation and phase shift of EM wave in different radial depths (Hizem et al., 2008). Successful field tests have been reported that the tool can simultaneously inverse the permittivity and conductivity of the virgin formation (Mosse et al., 2009). Once the prior information of formation permittivity is acquired with the mentioned methods, the wave velocity can be calculated, and thus the water front distance can be converted from the two-way traveltime of reflected signals.

PRODUCTION CONTROLS COMBINED WITH BOREHOLE RADARS

Reservoir imaging with radar array

This section investigates the capability of borehole radar array for reservoir imaging and develops a valve control method combined with radar imaging results. To assess the practical superiority of borehole radar monitoring reservoir, a production strategy, supported by our borehole radar, is quantitatively compared with a proportional reactive control strategy and an uncontrolled conventional well production.

A conceptual reservoir model (labeled as model 2) is used in this section. It is a typical reservoir scenario produced by a horizontal well under the drive of strong bottom water pressure, as depicted in

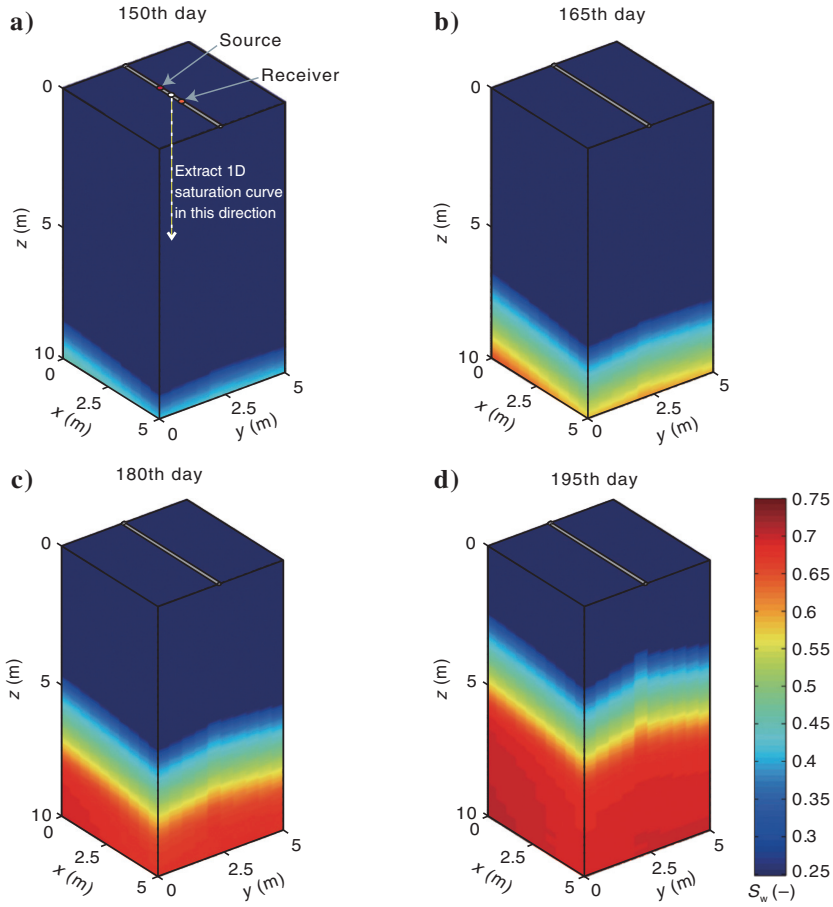

Figure 5. Snapshots of water saturation distributions in the extracted box volume on the (a) 150th day, (b) 165th day, (c) 180th day, and (d) 195th day of production, respectively. The red part represents the invading water and the blue part the oil in-place.

Downloaded 01/25/18 to 131.180.130.242. Redistribution subject to SEG license or copyright; see Terms of Use at http://library.seg.org/

Figure 8. This model is a simplified representation of a thin oil reservoir in Indiana, USA (Bryant et al., 2002), and it has been frequently used in smart well production studies (Raghuraman et al., 2003; Bryant et al., 2004; Addiego-Guevara et al., 2008; Dilib and Jackson, 2013). The model is 1828.8 m long, 944.88 m wide, and 30.48 m thick. The reservoir top is located at a depth of 1828.8 m, and the initial oil-water contact is at a depth of 1859.28 m. The reservoir contains water and oil, whereas gas is neglected. A horizontal well is located 10.67 m below the top shale layer for oil production. The well is segmented by two individual completions with a perforation length of 365.76 m for each. The primary parameters of reservoir and well are presented in Table 3. Capillary pressure is neglected, whereas wellbore friction is considered.

The model is characterized by a high-permeability channel across a low-permeability reservoir. The heterogeneous media will cause uneven water front movement, therefore giving rise to early water breakthrough. As analyzed before, the formation water content primarily controls the radar attenuation and thus the radar detection range (Miorali et al., 2011b). In this scenario, the well is located in the oil-bearing layer in which the oil saturation is considerably high (Figure 8 and Table 3), and therefore the distributions of water content have little variation with position relative to the distributions of

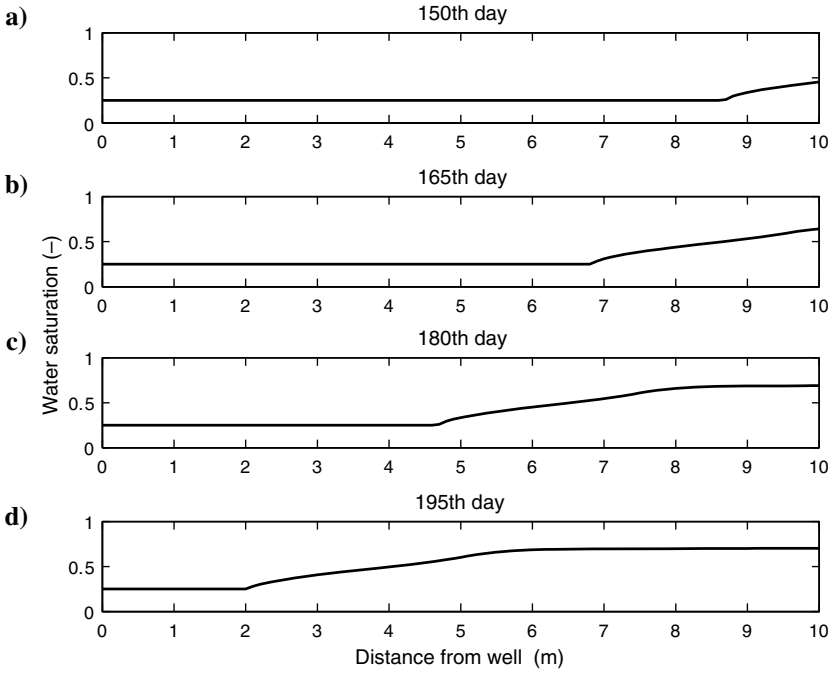

Figure 6. One-dimensional water saturation curves extracted from the saturated volume in Figure 5. The curves demonstrate the water front moving toward the well after (a) 150 days, (b) 165 days, (c) 180 days, and (d) 195 days of production, respectively.

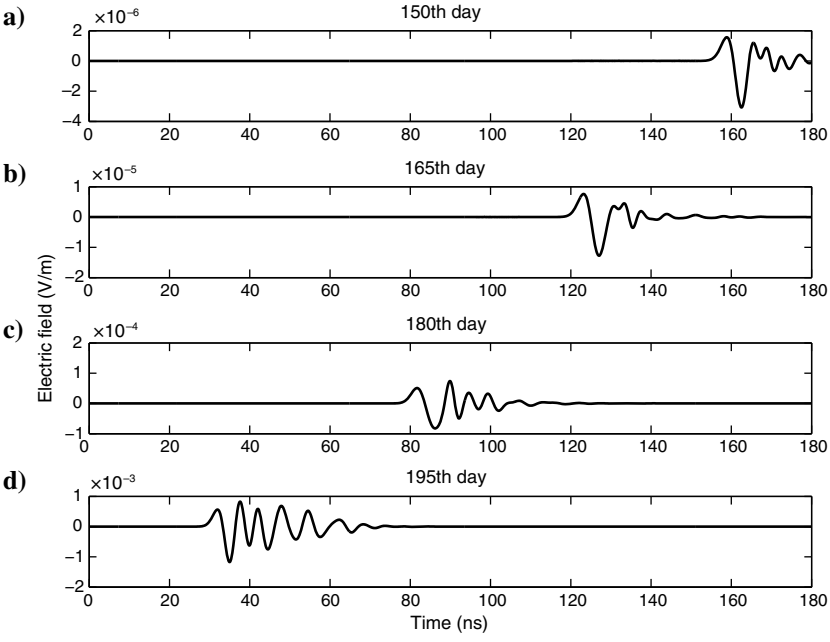

Figure 7. EM responses of 3D time-lapse GPR simulations on the 150th, 165th, 180th, and 195th day of oil production, respectively, corresponding to the water front movement shown in Figure 6.

Downloaded 01/25/18 to 131.180.130.242. Redistribution subject to SEG license or copyright; see Terms of Use at http://library.seg.org/

permeability and porosity. In view of these analyses, it can be safe to assume a uniform monitoring range (approximately 10 m) for the radar sensors in different well positions.

The reservoir simulations deploy a nonuniform meshing scheme similar to the previous model. The finely gridded portion below the first completion simulates a realistic oil-water transition zone, which is the region of our interest for GPR simulations. In the simulations of array radars, the antenna configurations, boundary condition setting, and gridding scheme are the same as the previous EM model. Multiple radar antennas are distributed along the wellbore with an adjacent space of 28 m (Figure 9a). A cluster of GPR traces (i.e., 1D time-lapse EM waveforms obtained by every individual receiver) are merged into a 2D image. Note that densely allocated sensors present a high spatial resolution for reservoir imaging, but the number of distributed sensors should be financially weighted specific to field applications. In addition, a small separation distance between the sensors is possible to arouse interference from the adjacent transmitters, but the time-lapse measurement can remove the undesired wavelets from the received signals. Figure 9 shows the snapshots of water saturation distributions in the region of interest when the water front is 8, 6, 4, and 2 m away from the well, corresponding to time-lapse radar images presented in Figure 10. The contrasts between Figures 9 and 10 reveal that the temporal envelopes of the radar images agree well with the spatial distributions of the water front, and therefore the water front profiles are approximately reconstructed by the borehole radar array.

Table 3. Reservoir and well properties for model 2.

Reservoir and well parameters		
Variables	Values	Units
Initial pressure at reference depth	24,800	kPa
Horizontal permeability	0.50	darcy
Vertical permeability (low)	0.01	darcy
Vertical permeability (high)	0.50	darcy
Porosity	0.25	—
Oil compressibility	2.10e-6	$(\text{kPa})^{-1}$
Water compressibility	4.35e-7	$(\text{kPa})^{-1}$
Water density	1000	kg/m^3
Oil density	800	kg/m^3
Water viscosity	5.00e-4	$\text{Pa} \cdot \text{s}$
Oil viscosity	3.40e-4	$\text{Pa} \cdot \text{s}$
Connate water saturation	0.25	—
Residual oil saturation	0.25	—
Water end-point relative permeability	0.80	—
Oil end-point relative permeability	0.80	—
Water Corey exponent	2	—
Oil Corey exponent	2	—
Aquifer strength	103.74e3	m^3/kPa
Aquifer compressibility	7.25e-7	$(\text{kPa})^{-1}$
Aquifer characteristic time	10	year
Well radius	0.14	m
Surface Liquid rate	1589.83	m^3/d

Production strategies

Three different production strategies, i.e., uncontrolled, reactive, and combined production strategies, are simulated. The simulations are confined in a production period of 10 years, which is approximately the production lifetime of this reservoir scenario. The wellhead production rate is fixed at 1589.83 m^3/d throughout the production. We assume no limitation on inflow capacity of each individual completion. The assumption excludes the constraint of minimum well bottom pressure and allows for a broad range of ICV regulations.

In the production case of no monitoring and control, the inflow rate in the first completion is greater than the second one. Therefore, early breakthrough inevitably occurs, and oil production is hampered. The phenomenon is primarily caused by the high-permeability streak, as indicated in Figure 8. In addition, higher pressure drawdown at the heel (the left of the well in Figure 8) than at the toe (the right of the well in Figure 8), arising from wellbore friction,

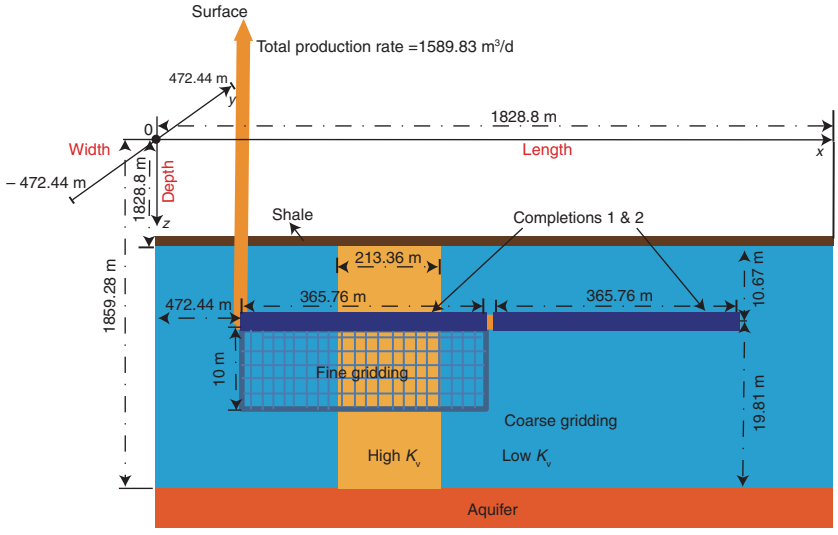

Figure 8. Parallel representation of the reservoir and well configurations of model 2 (Raghuraman et al., 2003).

speeds up the influx of fluids into the first completion, which is called the heel-toe effect (Jansen et al., 2002).

Before water breakthrough, the reactive production has the same segment inflow rates as the uncontrolled one. After water breakthrough, we use an empirical algorithm of proportional reactive control to relieve water invading, as described by (Addiego-Guevara, 2009)

$$\Pi_k = \mathrm{MIN}\left[\left(\frac{1 - WCT_k}{1 - WCT_{\min}}\right)^{\alpha}, 1\right], \tag{3}$$

where Π_k is the ICV choking coefficient for a given completion k, which is linked with the inflow rate of the corresponding completion, varying from 0, when ICV is fully closed, to 1, when the ICV is fully open; WCT_k stands for the water cut reading inside a given completion k; $WCT_{\min}$ is the lowest water cut reading among the completions; α is a constant factor specific to a production case, and it reflects the nonlinear correlations between the ICV choking velocity and the difference of the water cut readings among every completion. A strong nonlinearity signifies that the ICVs can be rapidly choked to maintain a relatively small difference of water cut readings among the segments. In this study, α is defined as 10.

In the third production strategy, we add a proactive control to the proportional reactive control, expecting to combine their advantages for greater benefit. In addition to multiphase flow meters, the well requires to be equipped with reservoir monitoring tools, which can

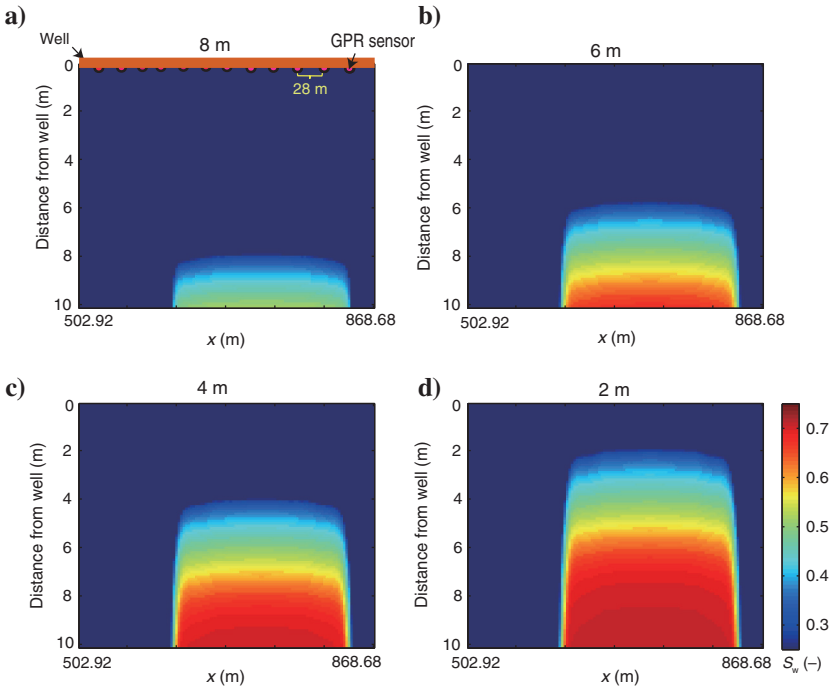

Figure 9. GPR sensors (red dots) distributed along the well and the snapshots of water saturations in the region of interest.

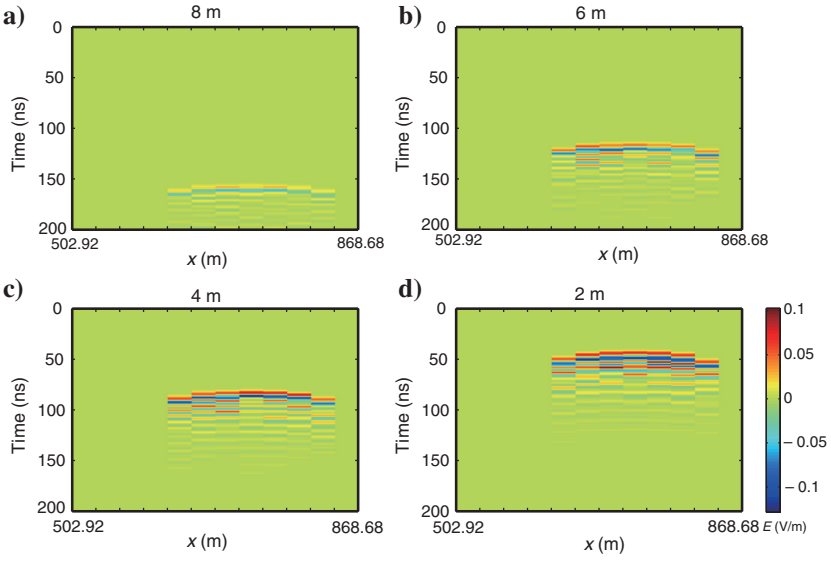

Figure 10. EM imaging results of time-lapse radar array measurements when water front is 8 m (Figure 9a), 6 m (Figure 9b), 4 m (Figure 9c), and 2 m (Figure 9d) away from the well.

Downloaded 01/25/18 to 131.180.130.242. Redistribution subject to SEG license or copyright; see Terms of Use at http://library.seg.org/

Downloaded 01/25/18 to 131.180.130.242. Redistribution subject to SEG license or copyright; see Terms of Use at http://library.seg.org/

be supported by our borehole radar imaging technology. The overall work flow of production and control is clarified in Figure 11. In the initial period of production, both ICVs are fully open. After the water approaches the detection range of borehole radars, proactive control is activated, and a feedback control is conducted by linking ICV choking with radar imaging data. After the water breaks through the well, proactive control is terminated and proportional reactive control is initiated until the well is shut.

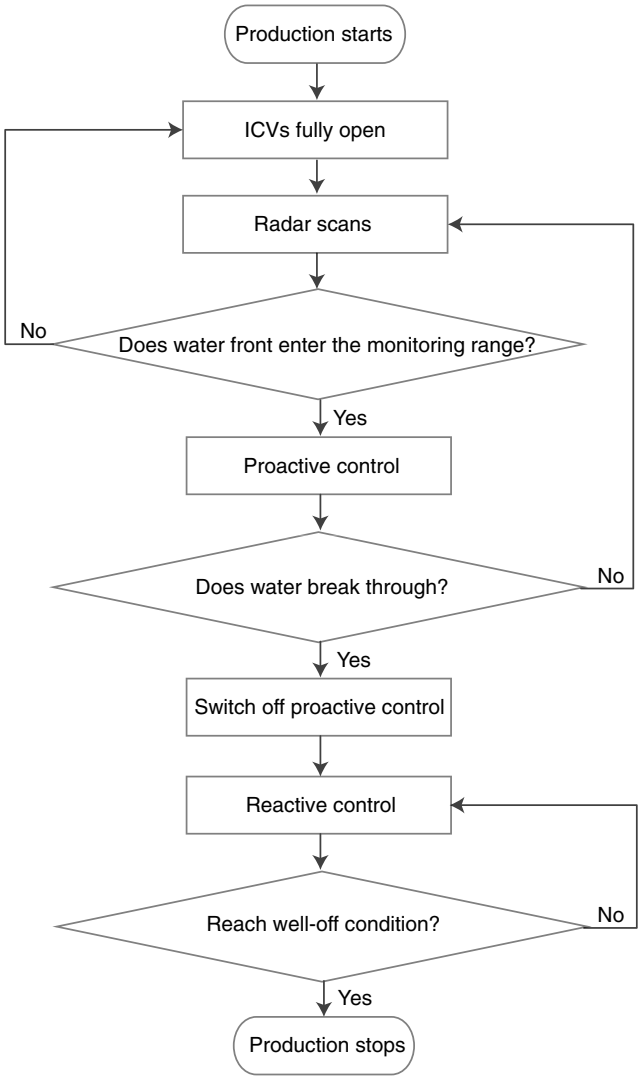

Figure 11. Flow diagram of the combined production strategy.

In the stage of proactive control, we set the period of monitoring and control as seven days. Every seven days, radar array implements a set of scanning to capture the profile of fluid flow, and then a control decision is made for ICV choking or maintaining. A simple proactive control algorithm is proposed in this study, as described by

$$\Pi_k^t = \begin{cases} \beta\Pi_k^{t-1}, & (\text{if } |D_k - D_{\max}| > D_{\text{th}}) \\ \Pi_k^{t-1}, & (\text{if } |D_k - D_{\max}| < D_{\text{th}}) \\ 1, & (\text{if } |D_k - D_{\max}| = 0) \end{cases} \tag{4}$$

where Π_k^t and Π_k^{t-1} represent the choking coefficients of the kth completion in the current and previous periods of monitoring and control, respectively, and β is the discount factor, reflecting the choking extent of ICVs relative to the previous period, and it is set as 0.5 in this study; D_k denotes the distance between the kth completion and its corresponding leading displacement edge, and it can be obtained by searching the minimum traveltime of reflected waves in the corresponding radar trace gather; $D_{\max}$ is the maximum value among all the D_ks, which corresponds to the slowest flow zone; and D_{th} is the threshold that links the distance difference of the water front to the proactive action, reflecting the tolerance extent of proactive controls to the unevenness of the water front profile, and it is set as 1 m in this case. For dual-completion smart well production, the procedure of proactive control by this formula is described as follows: (1) After water invades the monitoring range (i.e., 10 m away from the well), proactive control is started. (2) If the water front in one completion zone moves above 1 m ahead of that in the other, the corresponding ICV is choked back at a discount factor of 0.5 to reduce its ICV inflow, and meanwhile the other completion keeps its ICV fully open. (3) If the distance difference of the water front in the two zones is within 1 m, both completions maintain their ICVs unchanged until the next period. The basic principle of the proactive control algorithm is to slow down the production in the faster flowing zone while speeding up the production in the slower one, in order to gradually flatten the water front profile. Although we adopt a well with two completions

Figure 12. Wellhead production rates of water and oil for the three production strategies.

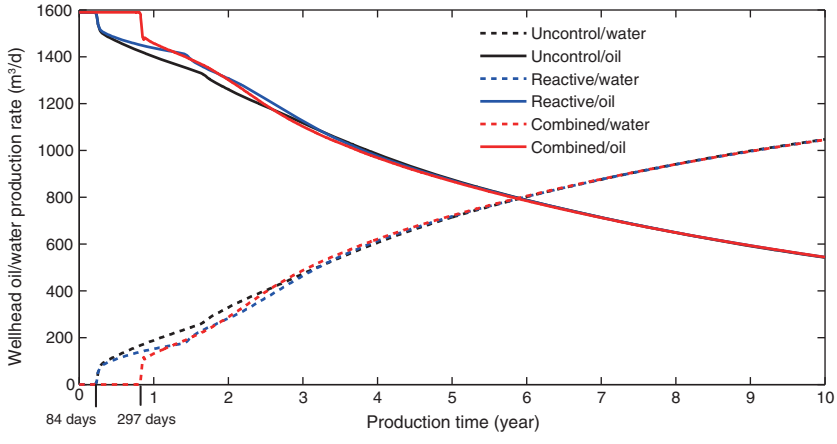

Downloaded 01/25/18 to 131.180.130.242. Redistribution subject to SEG license or copyright; see Terms of Use at http://library.seg.org/

in this scenario, the algorithm is also expected to suit multisegment smart well systems.

Figure 12 records the wellhead production rates of oil and water by the three production strategies. For the conventional and reactive production strategies, there is a water-free production period of 84 days. Afterward, water breaks through the well, and the wellhead oil production rate is decreased whereas the water production rate is increased. However, after water breakthrough, the reactive production strategy still maintains a higher oil production rate and lower water production rate than the conventional well production for a long period. The combined production strategy delays the water breakthrough time for 213 days relative to the reactive production, thereby keeping a water-free production period of approximately 10 months. After the combined production encounters water breakthrough, it holds similar oil and water production rates as the reactive production because of the subsequent reactive behavior.

Figures 13 and 14 respectively show the inflow rates and water front distances of each completion by the combined production strategy. After water approaches the monitoring range, the proactive control decreases the flow rate of completion 1 until it is close to zero, whereas the flow rate of completion 2 increases due to the constant wellhead liquid rate (Figure 13). In this stage, water front movement in completion 1 zone is slowed down until it is caught up with by the moving water front in completion 2 zone (Figure 14). The effects of the proactive control can be summarized as follows: (1) balancing inflow rates of each completion and flattening water front profile, (2) delaying water breakthrough, and (3) improving sweep efficiency. Figure 15 presents the snapshots of saturation distributions after 270 days of production by the reactive and combined production strategies, respectively. We can see that, after water breakthrough has occurred in the reactive production strategy, water is still far away from the well in the combined production strategy. The obvious delay of water breakthrough is attributed to proactive control behaviors.

Table 4 sums up the cumulative productions of water and oil by the three production strategies and their relative improvement percentages. Data are recorded and compared in the production periods of one year, five years, and ten years, respectively, implying a short-term, mid-term, and long-term optimization effects. Compared with the conventional well production, the reactive production strategy and the combined production strategy improve cumulative oil production and decrease cumulative water production in every production period. Relative to the reactive production strategy, the combined production strategy further decreases cumulative water production by 66.89%, 1.75%, and 0.45%, and it increases cumulative oil production by 4.76%, 0.57%, and 0.31%, respectively, in the production periods of one year, five years, and ten years. The quantitative comparisons reveal that the combined production strategy is superior to the reactive production in accelerating oil production and suppressing water production, and its advantages are more remarkable in the early stage of production because proactive control delays water breakthrough with the help of borehole radar monitoring.

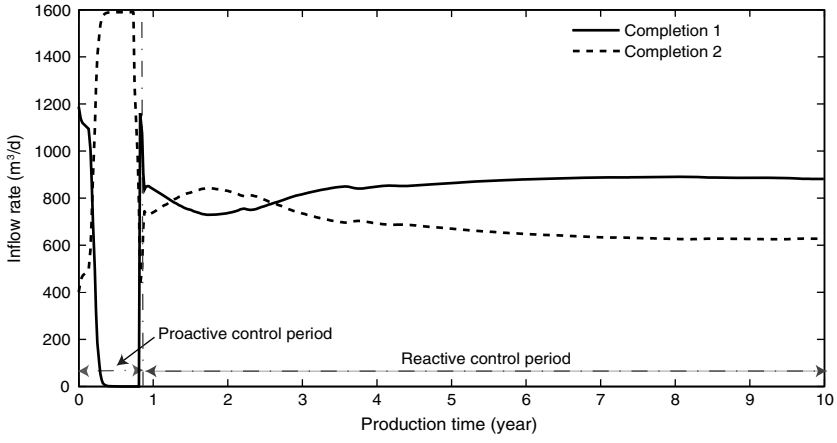

Figure 13. Liquid inflow rates of each completion for the combined production strategy.

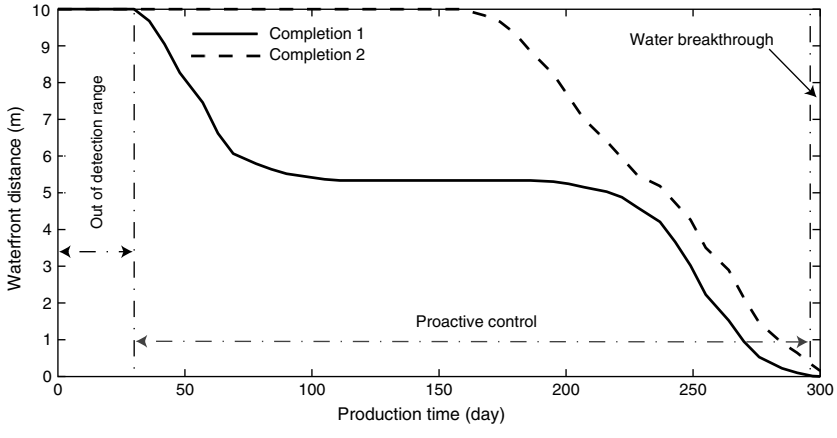

Figure 14. Water front distance from the well in each completion zone for the combined production strategy.

Downloaded 01/25/18 to 131.180.130.242. Redistribution subject to SEG license or copyright; see Terms of Use at http://library.seg.org/

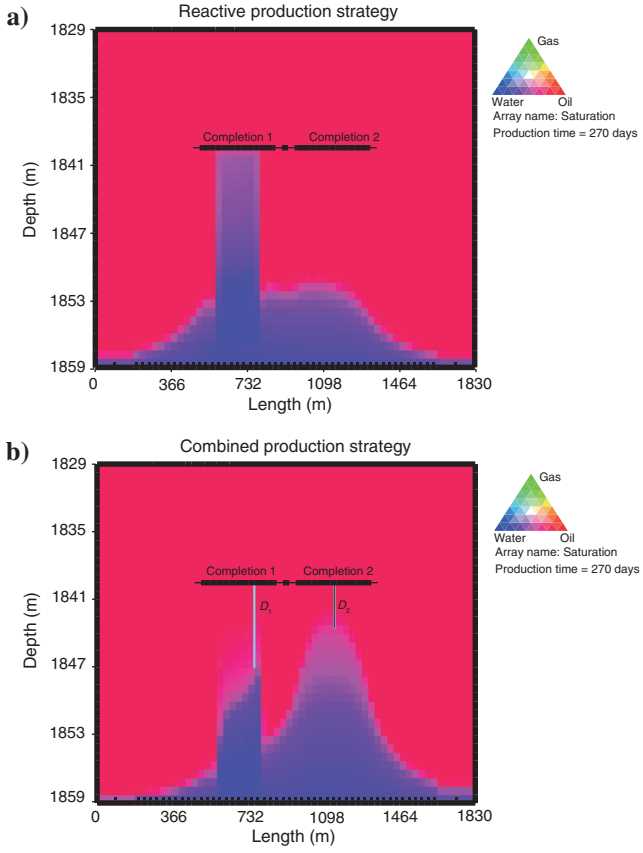

Figure 15. Snapshots of saturation distributions after 270 days of production for (a) the reactive and (b) combined production strategies simulated by MoReS. D_1 and D_2 represent the distances of displacement front away from completion 1 and completion 2, respectively.

Table 4. Cumulative production data and relative improvements for the three production strategies.

Production data			
Data recorded	Uncontrolled	Reactive	Combined
Production for 1 year			
Cumulative water production	3.8563×10^4 m^3	3.3200×10^4 m^3	7.4025×10^3 m^3
Decrease of water production	—	13.91%	80.80%
Cumulative oil production	5.4178×10^5 m^3	5.4714×10^5 m^3	5.7294×10^5 m^3
Increase of oil production	—	0.99%	5.75%
Production for 5 years			
Cumulative water production	7.1852×10^5 m^3	6.8901×10^5 m^3	6.7645×10^5 m^3
Decrease of water production	—	4.11%	5.86%
Cumulative oil production	2.1849×10^6 m^3	2.2145×10^6 m^3	2.2269×10^6 m^3
Increase of oil production	—	1.35%	1.92%
Production for 10 years			
Cumulative water production	2.3639×10^6 m^3	2.3340×10^6 m^3	2.3234×10^6 m^3
Decrease of water production	—	1.26%	1.71%
Cumulative oil production	3.4429×10^6 m^3	3.4728×10^6 m^3	3.4835×10^6 m^3
Increase of oil production	—	0.87%	1.18%

CONCLUSION

We establish an integrated 3D numerical model coupling EM propagation and multiphase fluid flowing, and we investigate the potential of borehole radar for reservoir monitoring in a smart well production environment. A box-scale simulation indicates that the reflected signals extracted from a time-lapse borehole radar measurement have good correspondence with the evolution of the oil-water front. Therefore, we conclude that borehole radar has a capability of detecting the changes of water and oil distributions in the near-well region of a production well. EM imaging simulations show that borehole radar arrays can reconstruct the profile of the water front in a bottom-water drive reservoir. We propose that the borehole radar array can be an effective downhole imaging tool to capture the comprehensive information of fluid dynamics in a produced reservoir.

Based on imaging data fed back from radar array, a proactive control approach is conducted to regulate completion inflow rates in smart well production. The control scheme successfully delays the water breakthrough time, and it obviously extends water-free production period. To demonstrate the practical advantages of borehole radar for oil industries, we simulate three production strategies in a thin oil reservoir produced by a horizontal well. The comparisons of production data in different production stages imply that the production strategy combining the reactive and proactive controls, which is supported by our borehole radar monitoring, can accelerate oil production and suppress water production, and that more superiority resides in short-term rather than long-term optimizations. The increase of cumulative oil will make more profits, whereas the decrease of cumulative water can save the costs of water handling. Especially, the noticeable improvement in the early production stage can accelerate the return of investment, showing an economic attraction for oil industries.

We suggest that borehole radar is a promising downhole sensor for reservoir monitoring, and it has the potential to improve recovery efficiency if combined with a proper production control strategy. The ideal application environments are thin oil reservoirs produced with the bottom-water drive. Further studies should be carried out on the selection of the reservoir types in which borehole radar monitoring can take effects, and more advanced smart well control algorithms are to be developed to gain more benefits. For field applications, antenna design and hardware manufacture are also vital.

ACKNOWLEDGMENTS

This research was supported by the ISAPP (Integrated System Approach Petroleum Production) project cooperated by Shell Global Solutions International BV, Delft University of Technology, and Netherlands Organisation for Applied Research (TNO), the National Natural Science Foundation of China (no. 41674138), and the Fundamental Research Funds for the Central Universities, China University of Geosciences (no. CUG160211). We thank A. Giannopoulos, University of Edinburgh, UK, for usage of

Downloaded 01/25/18 to 131.180.130.242. Redistribution subject to SEG license or copyright; see Terms of Use at http://library.seg.org/

GprMax, and E. Addiego-Guevara for providing MoReS templates to simulate smart well production. We thank Shell for the permission to use the reservoir simulator in the framework of ISAPP.

REFERENCES

Addiego-Guevara, E., 2009, Quantifying the value of reactive and proactive feedback control strategies for intelligent wells: Ph.D. thesis, Imperial College London.

Addiego-Guevara, E., M. D. Jackson, and M. A. Giddins, 2008, Insurance value of intelligent well technology against reservoir uncertainty: Presented at the Symposium on Improved Oil Recovery, SPE.

Aggrey, G. H., D. R. Davies, and L. T. Skarsholt, 2007, A novel approach of detecting water influx time in multi-zone and multi-lateral completions using real-time downhole pressure data: Presented at the Middle East Oil and Gas Show and Conference, SPE.

Archie, G. E., 1942, The electrical resistivity log as an aid in determining some reservoir characteristics: Transactions of the American Institute of Mining Engineers, **146**, 54–62, doi: 10.2118/942054-G.

Birchak, J. R., C. G. Gardner, J. E. Hipp, and J. M. Victor, 1974, High dielectric constant microwave probes for sensing soil moisture: Proceedings of the IEEE, **62**, 93–98, doi: 10.1109/PROC.1974.9388.

Black, A., J. Hare, and J. MacQueen, 2016, Borehole gravity monitoring in the aquistore CO_2 sequestration well: 86th Annual International Meeting, SEG, Expanded Abstracts, 768–772.

Bryant, I. D., M. Y. Chen, B. Raghuraman, I. Raw, J. P. Delhomme, C. Chouzenoux, D. Pohl, Y. Manin, E. Rioufol, and G. Oddie, 2002, An application of cemented resistivity arrays to monitor waterflooding of the Mansfield Sandstone, Indiana, USA: SPE Reservoir Evaluation and Engineering, **5**, 447–454, doi: 10.2118/81752-PA.

Bryant, I. D., M. Y. Chen, B. Raghuraman, R. Schroeder, M. Supp, J. Navarro, I. Raw, J. Smith, and M. Scaggs, 2004, Real-time monitoring and control of water influx to a horizontal well using advanced completion equipped with permanent sensors: SPE Drilling and Completion, **19**, 253–264, doi: 10.2118/77522-PA.

Butler, R. M., 1991, Thermal recovery of oil and bitumen: Prentice Hall Inc.

Chen, Y. H., and M. L. Oristaglio, 2002, A modeling study of borehole radar for oil-field applications: Geophysics, **67**, 1486–1494, doi: 10.1190/1.1512793.

Daniels, D., D. Gunton, and H. Scott, 1988, Introduction to subsurface radar: IEE Proceedings F (Communications, Radar and Signal Processing), **135**, 278–320, doi: 10.1049/ip-f-1.1988.0038.

Dilib, F. A., and M. D. Jackson, 2013, Closed-loop feedback control for production optimization of intelligent wells under uncertainty: SPE Production and Operations, **28**, 345–357, doi: 10.2118/150096-PA.

Dilib, F. A., M. D. Jackson, A. M. Zadeh, R. Aasheim, K. Årland, A. J. Gyllensten, and S. M. Erlandsen, 2015, Closed-loop feedback control in intelligent wells: Application to a heterogeneous thin oil-rim reservoir in the North Sea: SPE Reservoir Evaluation and Engineering, **18**, 69–83, doi: 10.2118/159550-PA.

Donadille, J. M., and O. Faivre, 2015, Water complex permittivity model for dielectric logging: Presented at the Middle East Oil & Gas Show and Conference, SPE.

Dyer, S., Y. El-Khazindar, A. Reyes, M. Huber, I. Raw, and D. Reed, 2007, Intelligent completions — A hands-off management style: Oilfield review, **19**, 4–17.

Ebadi, F., and D. R. Davies, 2006, Should "proactive" or "reactive" control be chosen for intelligent well management?: Presented at the Intelligent Energy Conference and Exhibition, SPE.

Ellefsen, K. J., A. T. Mazzella, R. J. Horton, and J. R. Mckenna, 2011, Phase and amplitude inversion of crosswell radar data: Geophysics, **76**, no. 3, J1–J12, doi: 10.1190/1.3554412.

Elmsallati, S. M., D. R. Davies, and S. M. Erlandsen, 2005, A case study of value generation with intelligent well technology in a high productivity, thin oil rim reservoir: Presented at the Middle East Oil and Gas Show and Conference, SPE.

Gagliardi, P., and D. C. Lawton, 2012, Orientation analysis of borehole geophones: Calibration consistency: 82th Annual International Meeting, SEG, Expanded Abstracts, 1–5.

Giannopoulos, A., 2005, Modelling ground penetrating radar by GprMax: Construction and Building Materials, **19**, 755–762, doi: 10.1016/j.conbuildmat.2005.06.007.

Glandt, C. A., 2005, Reservoir management employing smart wells: A review: SPE Drilling and Completion, **20**, 281–288, doi: 10.2118/81107-PA.

Guo, C., and R. C. Liu, 2010, A borehole imaging method using electromagnetic short pulse in oil-based mud: IEEE Geoscience and Remote Sensing Letters, **7**, 856–860, doi: 10.1109/LGRS.2010.2049638.

Heigl, W. M., and M. Peeters, 2005, Can we obtain invasion depth with directional borehole radar?: Petrophysics, **46**, 52–61.

Hizem, M., H. Budan, B. Deville, O. Faivre, L. Mosse, and M. Simon, 2008, Dielectric dispersion: A new wireline petrophysical measurement: Presented at the Annual Technical Conference and Exhibition, SPE.

Huisman, J., S. Hubbard, J. Redman, and A. Annan, 2003, Measuring soil water content with ground penetrating radar: Vadose Zone Journal, **2**, 476–491, doi: 10.2136/vzj2003.4760.

Jansen, J. D., A. M. Wagenvoort, V. S. Droppert, R. Daling, and C. A. Glandt, 2002, Smart well solutions for thin oil rims: Inflow switching and the smart stinger completion: Presented at the Asia Pacific Oil and Gas Conference and Exhibition, SPE.

Konopczynski, M., and A. Ajayi, 2004, Design of intelligent well downhole valves for adjustable flow control: Presented at the Annual Technical Conference and Exhibition, SPE.

Kragas, T. K., F. X. Bostick, C. Mayeu, D. L. Gysling, and A. M. V. D. Spek, 2003, Downhole fiber-optic flowmeter: Design, operating principle, testing, and field installations: SPE Production and Facilities, **18**, 257–268, doi: 10.2118/87086-PA.

Kuroda, S., H. Jang, and H. Kim, 2009, Time-lapse borehole radar monitoring of an infiltration experiment in the vadose zone: Journal of Applied Geophysics, **67**, 361–366, doi: 10.1016/j.jappgeo.2008.07.005.

Liang, H. Y., H. C. Yang, J. Hou, and L. Y. Cai, 2013, A compact ferrite-based dipole directional antenna for borehole radar application: IEEE Geoscience and Remote Sensing Letters, **10**, 486–489, doi: 10.1109/LGRS.2012.2210671.

Lumley, D. E., 2001, Time-lapse seismic reservoir monitoring: Geophysics, **66**, 50–53, doi: 10.1190/1.1444921.

Ma, C., Q. Zhao, J. Huo, X. Chang, and L. Ran, 2016, Single borehole radar for well logging in a limestone formation: Experiments and simulations: Journal of Environmental and Engineering Geophysics, **21**, 201–213, doi: 10.2113/JEEG21.4.201.

Miorali, M., E. Slob, and R. Arts, 2011a, A feasibility study of borehole radar as a permanent downhole sensor: Geophysical Prospecting, **59**, 120–131, doi: 10.1111/j.1365-2478.2010.00904.x.

Miorali, M., F. Zhou, E. Slob, and R. Arts, 2011b, Coupling ground penetrating radar and fluid flow modeling for oilfield monitoring applications: Geophysics, **76**, no. 3, A21–A25, doi: 10.1190/1.3569580.

Mosse, L., R. Carmona, E. Decoster, O. Faivre, and M. Hizem, 2009, Dielectric dispersion logging in heavy oil: A case study from the Orinoco Belt: Presented at the 50th Annual Logging Symposium, SPWLA.

Oloumi, D., M. I. Pettersson, P. Mousavi, and K. Rambabu, 2015, Imaging of oil-well perforations using UWB synthetic aperture radar: IEEE Transactions on Geoscience and Remote Sensing, **53**, 4510–4520, doi: 10.1109/TGRS.2015.2400918.

Poel, R. V. D., and J. D. Jansen, 2004, Probabilistic analysis of the value of a smart well for sequential production of a stacked reservoir: Journal of Petroleum Science and Engineering, **44**, 155–172, doi: 10.1016/j.petrol.2004.02.012.

Raghuraman, B., B. Couet, P. M. Savundararaj, W. J. Bailey, and D. J. Wilkinson, 2003, Valuation of technology and information for reservoir risk management: SPE Reservoir Evaluation and Engineering, **6**, 307–316, doi: 10.2118/86568-PA.

Regtien, J. M. M., M. T. van Stiphout, and F. F. van der Vlugt, 1995, Interactive reservoir simulation: Presented at the 13th Reservoir Simulation Symposium, SPE.

Reitz, A., R. Krahenbuhl, and Y. Li, 2015, Feasibility of time-lapse gravity and gravity gradiometry monitoring for steam-assisted gravity drainage reservoirs: Geophysics, **80**, no. 2, WA99–WA111, doi: 10.1190/geo2014-0217.1.

Ren, Y., Y. Wang, M. Wang, S. Wu, and B. Wei, 2014, A measuring system for well logging attitude and a method of sensor calibration: Sensors, **14**, 9256–9270, doi: 10.3390/s140509256.

Sato, M., and T. Takayama, 2007, A novel directional borehole radar system using optical electric field sensors: IEEE Transactions on Geoscience and Remote Sensing, **45**, 2529–2535, doi: 10.1109/TGRS.2007.898421.

Saunders, J. H., M. D. Jackson, M. Y. Gulamali, J. Vinogradov, and C. C. Pain, 2012, Streaming potentials at hydrocarbon reservoir conditions: Geophysics, **77**, no. 1, E77–E90, doi: 10.1190/geo2011-0068.1.

Shen, L. C., 1985, A laboratory technique for measuring dielectric properties of core samples at ultrahigh frequencies: SPE Journal, **25**, 502–514, doi: 10.2118/12552-PA.

Silva, M. F., K. M. Muradov, and D. R. Davies, 2012, Review, analysis and comparison of intelligent well monitoring systems: Presented at the Intelligent Energy International, SPE.

Talley, J., G. S. Baker, M. W. Becker, and N. Beyrle, 2005, Four dimensional mapping of tracer channelization in subhorizontal bedrock fractures using surface ground penetrating radar: Geophysical Research Letters, **32**, n/a–n/a, doi: 10.1029/2004GL021974.

Tronicke, J., and G. Hamann, 2014, Vertical radar profiling: Combined analysis of traveltimes, amplitudes, and reflections: Geophysics, **79**, no. 4, H23–H35, doi: 10.1190/geo2013-0428.1.

Tsoflias, G. P., T. Halihan, and J. M. Sharp, 2001, Monitoring pumping test response in a fractured aquifer using ground-penetrating radar: Water Resources Research, **37**, 1221–1229, doi: 10.1029/2000WR900297.

van Dongen, K. W., R. van Waard, S. van der Baan, P. M. van den Berg, and J. T. Fokkema, 2002, A directional borehole radar system: Subsurface Sensing Technologies and Applications, **3**, 327–346, doi: 10.1023/A:1020365414569.

Verbruggen, M. H. W., 2005, Influence of permeability and porosity variations on horizontal well behaviour: Application of geostatistical modelling on reservoirs in the Nimr field: Technical report, Shell International Exploration and Production Inc.

Vinogradov, J., and M. D. Jackson, 2011, Multiphase streaming potential in sandstones saturated with gas/brine and oil/brine during drainage and imbibition: Geophysical Research Letters, **38**, L01301, doi: 10.1029/2010GL045726.

Watts, G., T. Griffin, O. Barkved, and D. Foster, 2006, Seismic surveillance in the field of the future: Presented at the Intelligent Energy Conference and Exhibition, SPE.

Webster, M. J., S. M. Richardson, C. Gabard-Cuoq, J. Fitzgerald, and K. E. Stephenson, 2006, Well surveillance with a permanent downhole multiphase flowmeter: SPE Production and Operations, **21**, 388–393, doi: 10.2118/90024-PA.

Yang, H., T. Li, N. Li, Z. He, and Q. H. Liu, 2015, Efficient near-field imaging for single-borehole radar with widely separated transceivers: IEEE Transactions on Geoscience and Remote Sensing, **53**, 5327–5337, doi: 10.1109/TGRS.2015.2421478.

Zhao, J. G., and M. Sato, 2006, Radar polarimetry analysis applied to single-hole fully polarimetric borehole radar: IEEE Transactions on Geoscience and Remote Sensing, **44**, 3547–3554, doi: 10.1109/TGRS.2006.882260.

Zhao, J. G., and M. Sato, 2007, Consistency analysis of subsurface fracture characterization using different polarimetry techniques by a borehole radar: IEEE Geoscience and Remote Sensing Letters, **4**, 359–363, doi: 10.1109/LGRS.2007.895729.

Zhao, J. G., and M. Sato, 2008, Experimental implementation and assessment of two polarimetric calibration approaches applied for a fully polarimetric borehole radar: Journal of Geophysics and Engineering, **5**, 232–243, doi: 10.1088/1742-2132/5/2/010.

Zhou, F., X. Hu, and J. Liu, 2015, Comparative study of feedback control policies in water flooding production: Journal of Natural Gas Science and Engineering, **27**, 1348–1356, doi: 10.1016/j.jngse.2015.09.020.

Zhou, H., and M. Sato, 2000, Application of vertical radar profiling technique to Sendai Castle: Geophysics, **65**, 533–539, doi: 10.1190/1.1444748.

Zhou, H., and M. Sato, 2004, Subsurface cavity imaging by crosshole borehole radar measurements: IEEE Transactions on Geoscience and Remote Sensing, **42**, 335–341, doi: 10.1109/TGRS.2003.817215.

Downloaded 01/25/18 to 131.180.130.242. Redistribution subject to SEG license or copyright; see Terms of Use at http://library.seg.org/